# American Society of Mechanical Engineers

## ASME Accepted Manuscript Repository

**Institutional Repository Cover Sheet**

# A Benchmark Study of Modeling Lamb Wave Scattering by a Through Hole Using a Time-domain Spectral Element Method

*Menglong LIU[a]\*, David SCHMICKER[b], Zhongqing SU[c]\*, Fangsen CUI[a]*

[a]Institute of High Performance Computing, A\*STAR, Singapore 138632, Singapore

[b]Institute for Mechanics, Otto-von-Guericke University of Magdeburg, 39106 Magdeburg, Germany

[c]Department of Mechanical Engineering, The Hong Kong Polytechnic University, Hong Kong, P.R. China

\* To whom correspondence should be addressed. Tel.: +65-64191130, Email: liu_menglong@ihpc.a-star.edu.sg (Dr. Menglong LIU)

\* To whom correspondence should be addressed. Tel.: +852-2766-7818, Fax: +852-2365-4703, Email: Zhongqing.Su@polyu.edu.hk (Prof. Zhongqing SU, *Ph.D.*)

19     **Abstract**

20     Ultrasonic guided waves are being extensively investigated and applied to nondestructive

21     evaluation (NDE) and structural health monitoring (SHM). Guided waves are, under most

22     circumstances, excited in a frequency range up to several hundred kilohertz or megahertz for

23     detecting defect/damage effectively. In this regard, numerical simulation using finite element

24     analysis (FEA) offers a powerful tool to study the interaction between wave and defect/damage.

25     Nevertheless, the simulation, based on linear/quadratic interpolation, may be inaccurate to

26     depict the complex wave mode shape. Moreover, the mass lumping technique used in FEA for

27     diagonalizing mass matrix in the explicit time integration may also undermine the calculation

28     accuracy. In recognition of this, a time domain spectral element method (SEM) – a high-order

29     FEA with Gauss-Lobatto-Legendre node distribution and Lobatto quadrature algorithm – is

30     studied to accurately model wave propagation. To start with, a simplified two-dimensional

31     plane strain model of Lamb wave propagation is developed using SEM. The group velocity of

32     the fundamental anti-symmetric mode ($A_0$) is extracted as indicator of accuracy, where SEM

33     exhibits a trend of quick convergence rate and high calculation accuracy. A benchmark study of

34     calculation accuracy and efficiency using SEM is accomplished. To further extend SEM-based

35     simulation to interpret wave propagation in structures of complex geometry, a 3-D SEM model

36     with arbitrary in-plane geometry is developed. 3-D numerical simulation is conducted in which

37     the scattering of $A_0$ mode by a through hole is interrogated, showing a good match with

38     experimental and analytical results.

39

40
41     *Keywords:* Nondestructive evaluation; Structural health monitoring; Wave scattering; Spectral

42     element method; Lamb wave; finite element analysis

43

## 1. Introduction

Guided wave (GW)-based techniques in the field of NDE and SHM are promising to interrogate and detect structural defect/damage [1-3]. Several advantages of GW, including high sensitivity to damage, long propagation distance to cover large monitoring area with few sensors, and ability of system integration into the host structure with little additional penalty, endow the GW-based techniques with an online and *in situ* monitoring capability to various structures including aircraft, spacecraft, nuclear power plant, pipeline, etc. [4-8].

Currently most GW-based techniques rely on the extraction of limited parameters such as Time-of-flight and signal amplitude to identify damage size and location [2, 9]. In order to make full use of this technology, a fundamental physical interrogation on interaction of GW with various defect/damage is essential. Thus analytical analysis, together with numerical modeling, plays an important role of understanding GW in hope of extraction of more parameters. Nevertheless, when the geometric structure is complex, analytical analysis may not be applicable, which leaves the numerical modeling the only available method to accommodate complex geometric shapes. Among common numerical methods [10-14], finite element analysis (FEA) is dominantly adopted to analyze wave propagation as FEA has a strong adaptability to complex geometric shapes. Nevertheless, as conventional FEA uses linear/quadratic interpolation functions to represent coordinate and displacement, it may be inaccurate to depict the complex wave mode shape. Moreover, mass lumping technique is often adopted in the explicit time integration to obtain a diagonalized mass matrix. In this way, the calculation efficiency is improved, but at the cost of sacrificing calculation accuracy.

To enable a more accurate calculation, time-domain spectral element method (SEM) was proposed and applied to the modeling of wave propagation. Firstly developed by Patera to solve

69     laminar flow in a channel expansion in the mid-1980s, SEM is preferably used in problems

70     where FEA has a slow convergence rate [15]. Similar to FEA, SEM is also a weighted residual

71     method and subdivides the whole spatial domain into elements of finite sizes. Two main features

72     differentiating SEM from FEA are 1) elements in SEM have inner nodes and thus high-order

73     interpolation functions are adopted, and 2) SEM adopts a numerical integration rule called a

74     nodal quadrature, where integration points may coincide with nodal points. The first feature of

75     SEM reduces numerical dispersion errors because high-order interpolation functions present a

76     better geometric adaption to complex wave mode shapes than linear/quadratic interpolation

77     functions. The second feature generates a lumped mass matrix intrinsically by the nodal

78     quadrature without adopting any mass lumping technique. The explicit time integration is

79     dominantly used to solve the problem of wave propagation in SEM and commercial FEA

80     software packages. For the purpose of securing calculation efficiency, FEA usually adopts mass

81     lumping techniques, which force a full mass matrix diagonalized, but these techniques may

82     undermine the solution accuracy as a result of the approximation. Nevertheless, as SEM

83     intrinsically achieves a diagonalized mass matrix, the calculation accuracy will not be

84     compromised.

85

86     When Patera firstly developed SEM to solve the Navier-Stokes equation in fluid dynamics,

87     nodes follow a Chebyshev collocation, and it is concluded that SEM converges exponentially,

88     while FEA can only converge algebraically [15]. In 1990s, Komatisch introduced the so-called

89     Gauss-Lobatto-Legendre (GLL) node collation and Lobatto quadrature in SEM to efficiently

90     analyze the propagation of seismic wave [16]. Using the GLL-based node collation and Lobatto

91     quadrature, the mass matrix is intrinsically diagonalized, resulting in a significant improvement

92     of calculation accuracy. Consequently, less numerical error can be achieved using SEM

93     compared with conventional linear/quadratic FEA. Recently it is reported that a GPU-based

94    SEM was developed to a further speedup of 20 times compared with originally developed SEM

95    without the GPU acceleration [17]. Other main works about SEM for wave propagation involve

96    the application to composite [18] and the development of 2-D SEM membrane model and 3-D

97    SEM model respectively to study the interaction of in-plane waves with cracks [19, 20]. All

98    these investigations reported a significantly reduced calculation time and computational

99    resource consumption by using the SEM. Nevertheless, there are few intensive and quantitative

100   researches about the calculation accuracy of SEM. Zak systematically analyzed several error

101   sources of SEM while investigating longitudinal waves in the rod structure [21]. The influence

102   from node distributions, polynomial order and mass lumping techniques, was analyzed to give

103   an insightful mechanism of error generation and control. Although it is claimed that conclusions

104   from this work are not restricted only to the longitudinal wave in the rod, there entails more

105   intensive and quantitative analyses on the Lamb waves in the plate structures.

106

107   Another concern is that only the wave propagation in a relatively simple geometry is built and

108   solved using the current SEM techniques, such as the sphere structure representing the Earth

109   [17] and a notch representing the crack in a rectangular plate [19]. Lack of adaptation to

110   complex geometry shapes, the currently developed SEM technique is yet to be brought into a

111   broad application to practical problem. Addressing this concern, the development of SEM to

112   accommodate arbitrary geometry shape is of great significance to transform the theory of SEM

113   into practical technological application.

114

115   Addressing the above bottleneck and concern, a quantitative analysis into the calculation

116   accuracy of SEM, together with a development of 3-D SEM with arbitrary in-plane geometry,

117   is performed in this paper. Section 2 introduces the general principle of SEM and the

118   development procedure of a 3-D SEM model with arbitrary in-plane geometry. In Section 3, a

119     benchmark study of SEM is performed to quantitatively analyze the relation between

120     calculation accuracy with model parameters. The 3-D SEM model with arbitrary in-plane

121     geometry is built in Section 4, with the wave scattering from a through hole as example.

122     Concluding remarks are remunerated in Section 5.

123

124     **2.     Theory and Principle of SEM**

125     The basic principle of SEM is briefed in this section, with focus on the GLL-based node

126     collation and Lobatto quadrature. Then the development of 3-D SEM with arbitrary in-plane

127     geometry is explained.

128

129     **2.1     GLL-based Node Collation**

130     SEM differentiates from conventional linear/quadratic FEA in its forms of node collation. Two

131     forms of node collation are dominantly adopted for SEM, i.e., Chebyshev and GLL-based ones,

132     the latter of which is chosen in this study.

133

134     Supposing an SEM element in the direction with local coordinate $\xi \in [-1,1]$, Lobatto

135     polynomial $Lo_n(\xi)$, as the derivative of Legendre polynomial $P_{n+1}(\xi)$, is expressed as

136
$$Lo_n(\xi) = P'_{n+1}(\xi) = \frac{1}{2^{n+1}(n+1)!} \frac{d^{n+2}}{d\xi^{n+2}}[(\xi^2 - 1)^{n+1}]. \tag{1}$$

137     With polynomial order $p$, $Lo_p(\xi) = 0$ results in the zero points $\xi_0^{Lo_{p-1}}$, which, together with

138     two end points -1 and 1, constitute the GLL-based nodes in the $\xi$ direction with local

139     coordinates expressed as

140
$$\xi_i = \left\{ -1,\ \xi_0^{Lo_{p-1}}, 1 \right\}. \tag{2}$$

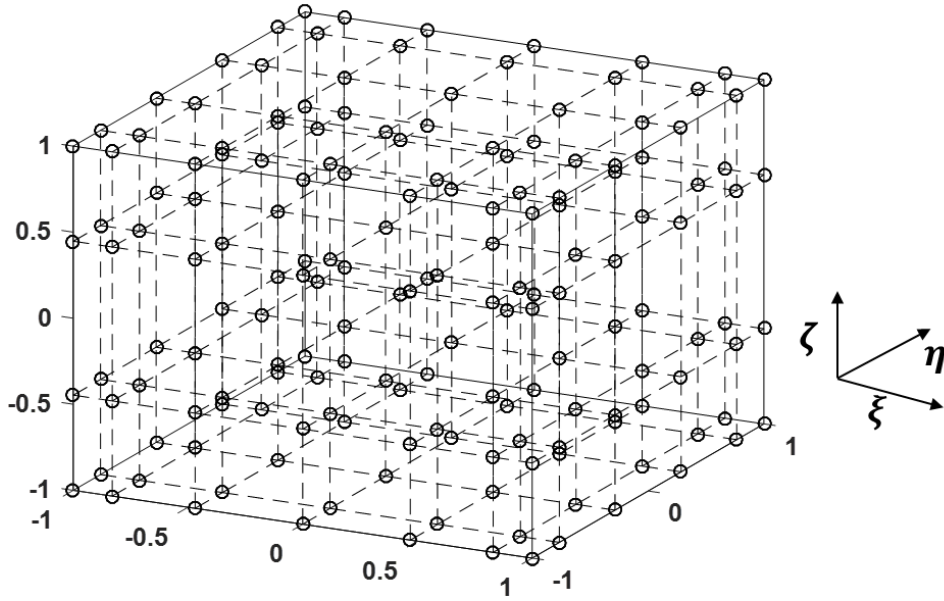141     Assuming a 3-D element with the polynomial order $p_\xi = 6$, $p_\eta = 5$ and $p_\zeta = 3$ in the three

142     directions $\xi$, $\eta$ and $\zeta$, the nodes in one SEM element are collated as displayed in Figure 1,

143    showing a non-uniform node collation. Lagrangian interpolation is adopted to further derive the

144    shape function $l_i^p(\xi)$ in the $\xi$ direction as

$$l_i^p(\xi) = \prod_{k=0, k \neq i}^{p} \frac{\xi - \xi_k}{\xi_i - \xi_k},$$     (3)

146    where $p$ is the polynomial order, and $i\ (i = 0, 1, ..., p)$ is the node number. The value of

147    Lagrangian interpolation with the GLL-based nodes when $p_\xi = 6$ is shown as Figure 2. It is

148    displayed that the maximum value of each Lagrangian interpolation is a constant value of 1 at

149    the corresponding nodes. Following the above procedure, the shape function of $D$-dimensional

150    element ($D$=1,2,3) can be derived through multiplication of Lagrangian interpolation functions

151    in respective directions.

152



153    Figure 1. GLL-based node collation in 3-D SEM element with the polynomial order $p_\xi = 6$,

154    $p_\eta = 5$ and $p_\zeta = 3$ in the local coordinate $\xi, \eta$, and $\zeta \in [-1, 1]$.
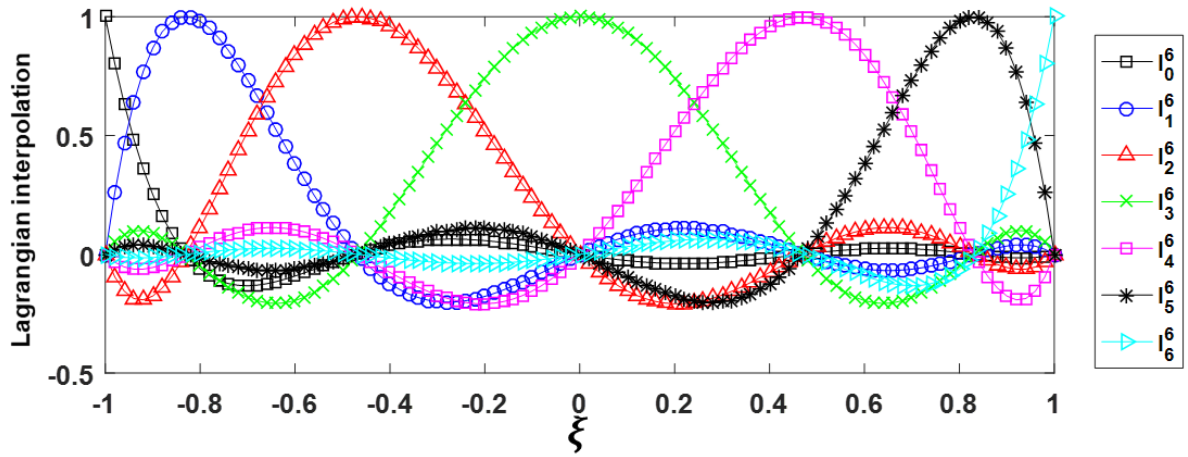
155

Figure 2. Lagrangian interpolation with polynomial order $p_\xi = 6$ of GLL nodes.

## 2.2  Dynamic Equation

When the entire geometrical domain is discretized into multiple solution sub-domains and assembled together, the global dynamic equation in the form of matrix is formed and then solved, to describe the structural response.

Without loss of generality, for a $D$-dimensional ($D = 1, 2, 3$) element with $N$ nodes, global coordinate $\boldsymbol{x}$ and displacement $\boldsymbol{u}$ can be denoted using the geometric and displacement shape functions $\boldsymbol{N_g}(\boldsymbol{\xi})$ and $\boldsymbol{N_d}(\boldsymbol{\xi})$ in the local coordinate, respectively, as

$$
\begin{aligned}
\boldsymbol{x} &= \sum_{k=1}^{N} \boldsymbol{N}_{g,k}(\boldsymbol{\xi})\boldsymbol{x}_k \\
\boldsymbol{u} &= \sum_{k=1}^{M} \boldsymbol{N}_{d,k}(\boldsymbol{\xi})\boldsymbol{u}_k
\end{aligned}
, \tag{4}
$$

where both shape functions are related with the Lagrangian interpolation in Equation (3). For the 2-D models analyzed in Section 3, $N = M$, the element is called isoparametric. While for the developed 3-D models as illustrated in Section 4, there may be $N < M$, and then the element is called subparametric.

173 With the above shape function to define coordinate and displacement, together with a series of

174 deductions involving dynamic equilibrium equation, stress-strain relation, and geometric

175 equation, the elemental mass and stiffness matrix can be obtained. The single element in the

176 elemental mass matrix, considering a $D$-dimensional model ($D = 1, 2, 3$) with $D$ displacement

177 degrees of freedom for each node, is expressed as

178
$$M_{ij}^e = \begin{cases} \rho \int_{V^e} N_{d,m}^2(\xi)dV, & i = j \\ \rho \int_{V^e} N_{d,n}(\xi)N_{d,o}(\xi)dV, \mod(i-j,D) = 0, i \neq j \\ 0, & \mod(i-j,D) \neq 0 \end{cases}$$
(5)

179 where $N_{d,m}$ denotes the displacement shape function at the $m^{th}$ node, $mod(i-j,D)$

180 denotes the remainder of $i - j$ to $D$, and $\rho$ and $V$ are density and volume, respectively. $m =$

181 ceil($i/D$), $n = $ ceil($i/D$), and $o = $ ceil($j/D$), where ceil($X$) denotes the operation to round

182 $X$ to the nearest integer greater than or equal to $X$.

183

184 All the elemental matrices are assembled to form the global dynamic equation expressed as

185
$$M\ddot{u} + Ku = f ,$$
(6)

186 where $M$, $K$, and $f$ are global mass matrix, global stiffness matrix, and global force vector,

187 respectively. The central difference method [22] is predominantly adopted to solve Equation

188 (6), in which the mass matrix $M$ will be inversed.

189

190 In the adopted SEM, mass matrix of the integral form in Equation (5) is calculated numerically

191 via the Lobatto quadrature algorithm, which is expressed as

192
$$\int_{-1}^{1} f(\xi)dx = \frac{2}{n(n-1)}[f(1) + f(-1)] + \sum_{i=2}^{n-1} w_i f(\xi_i) + R_n ,$$
(7)

193 where $f(\xi)$ denotes the function for quadrature, $n$ is the number of quadrature point, $w_i$ is

194 the weighting function, and $R_n$ the residue. When $n = p + 1$, the collation of quadrature

195    nodes coincides with the element nodes. Thus the second term in Equation (5), provided $R_n$ in

196    Equation (7) neglected, becomes zero. Consequently a diagonal mass matrix is intrinsically

197    generated, exerting a remarkable influence on the calculation accuracy. As stiffness matrix

198    cannot be diagonal, Gaussian quadrature is retained in this paper for the calculation of stiffness

199    matrix in SEM.

200

201    **2.3    Development of 3-D SEM**

202    To improve the adaptation to complex geometry, a 3-D SEM model with arbitrary in-plane

203    shape combining ABAQUS® and MATLAB® is built as illustrated in Figure 3. The procedure

204    is as follows.

205        1) The model parameters, including node number in one wavelength ($n_\lambda$) and

206            polynomial order ($p_\xi$, $p_\eta$ and $p_\zeta$) of SEM, are confirmed according to benchmark

207            study in Section 3.

208        2) ABAQUS® is introduced to discretize the in-plane structure into 2-D 8-node

209            biquadratic plane Serendipity elements [23].

210        3) MATLAB® is adopted for all the remaining calculation. 2-D in-plane SEM nodes

211            (see Figure 4) are collated according to ABAQUS® mesh and the polynomial orders

212            determined in Step 1. The global in-plane coordinate $(x_I, y_I)$ of node $I$ in the SEM

213            element is calculated as

$$(x_I, y_I) = \sum_{k=1}^{8} N_{g,k}(\xi_I, \eta_I) \cdot (x_k, y_k),  \tag{8}$$

215            where $N_{g,k}(\xi_I, \eta_I)$ denotes the shape function of Serendipity element at position with

216            local in-plane coordinate $(\xi_I, \eta_I)$ corresponding to the specified $I^{th}$ node in the SEM

217            element. $(x_k, y_k)$ is the global in-plane coordinate of the $k^{th}$ node in the ABAQUS®-

218            generated element.

219　　　4) The coordinate of out-of-plane SEM nodes $z_I$ (see Figure 4) is obtained according

220　　　　　to the polynomial order in the thickness direction $p_\zeta$ as

221
$$z_I = \frac{h}{2}\zeta_I,\qquad\qquad(9)$$

222　　　　　where $h$ is the plate thickness, $\zeta_I$ is the local coordinate in the thickness direction

223　　　　　corresponding to the specified $I^{th}$ node in the SEM element.

224　　　5) Construction of global mass, stiffness and force matrix to form dynamic equation.

225　　　6) Solution of dynamic equation using explicit integration algorithm.

226
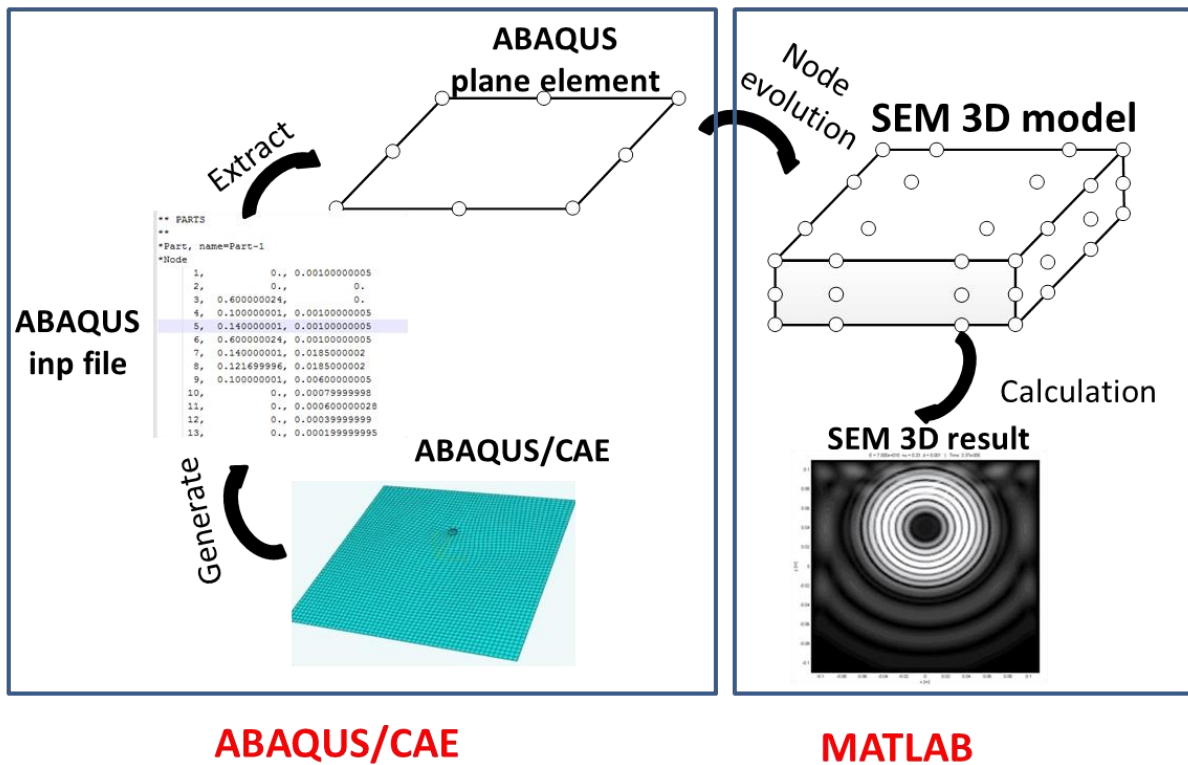


227

228　　　　　　　　　　Figure 3 Flowchart of development of 3-D SEM.

229

230　　As the material studied in this paper is isotropic, it is reasonable to set the same in-plane

231　　parameter, i.e. $p_\xi = p_\eta$. MATLAB® R2013a is adopted for the development of 2-D ABAQUS®

232　　mesh into 3-D SEM model and all the calculations. It is noteworthy that since in the in-plane

233　　direction, the geometry shape function is constructed from the initial ABAQUS® mesh

234    discretization (see Equation (8)), its polynomial order $N = 2$. Nevertheless, the displacement

235    shape function is constructed from the developed SEM node collation and thus the polynomial

236    order $M$ can be any integer equal to or over 2 (see Equation (4)).

237
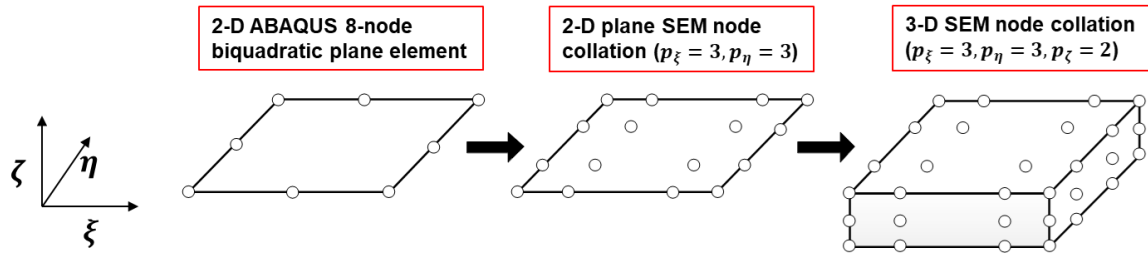


238

239    Figure 4. Illustration of SEM element built from ABAQUS$^{®}$ plane element ($p_\xi = 3, p_\eta =$

240    $3, p_\zeta = 2$, the shown element is represented in local coordinate $\xi$, $\eta$ and $\zeta \in [-1,1]$, and in

241    the global coordinate the element is usually irregular in order to adapt to complex geometry).

242

**3.    Benchmark Study on Calculation Accuracy of 2-D SEM**

244    A 2-D plane strain SEM model is built to simulate the GW propagation, whereby a benchmark

245    between calculation accuracy and efficiency of SEM in terms of various model parameters is

246    established in order to guide further modeling of both 2-D and 3-D cases.

247

**3.1    Model Description**

249        A 2-D plane strain SEM model is built with MATLAB$^{®}$ R2013a as illustrated in Figure 5.

250    To narrow down the frequency bandwidth of loading, a 32-cycle Hanning-window-modulated

251    sinusoidal signal with a central frequency $f_c = 100$ kHz is adopted as an in-plane force

252    loading $F_0$ at one node close to the left edge. The boundary reflection at the left edge is

253    eliminated through a symmetric boundary condition. Geometric parameters are listed in Table

254    1. And material parameters listed in

255    Table *2* are the same as [24] to perform a quantitative comparison of 3-D model in Section 4.

256    Table 3 lists the theoretical phase and group velocities of fundamental anti-symmetric mode

257    $A_0$ (central frequency $f_c = 20$ kHz and 100 kHz) with accuracy up to four decimal point.

258    Element size and node collation are varied according to three parameters, i.e., node number per

259    wavelength ($n_\lambda$) and polynomial order $p_\xi$ and $p_\eta$ in the in-plane and out-of-plane direction,

260    respectively. The arrival time of GW crossing sections A-B and C-D is recorded to calculate

261    wave group velocity, which, by comparison with theoretical group velocity, reflects the

262    calculation accuracy.
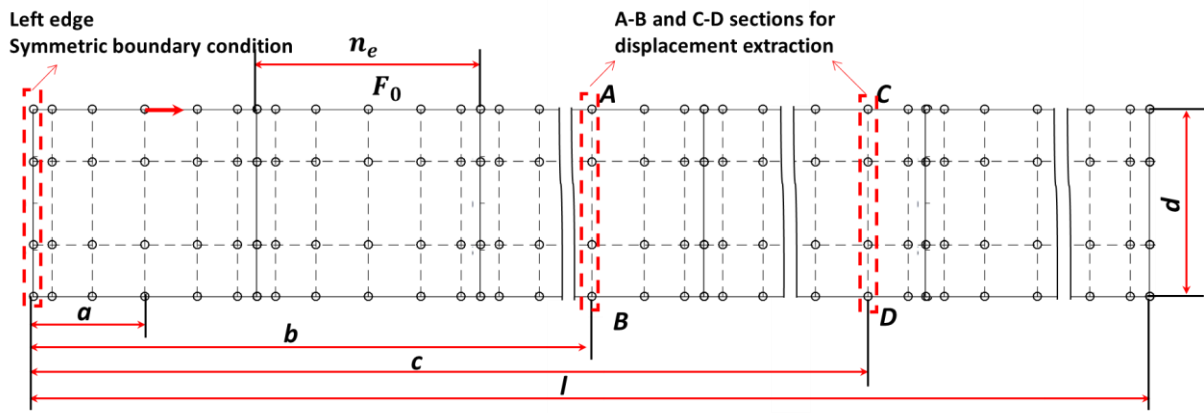
263



264    Figure 5. Element discretization and node collation of 2-D plane strain SEM model.

265

266    Table 1. Geometric parameters of 2-D plane strain SEM model.

| $a$ (mm) | $b$ (mm) | $c$ (mm) | $d$ (mm) | $l$ (mm) |
|---|---|---|---|---|
| 1 | 30 | 100 | 1 | 450 |

267

268    Table 2. Material parameters of both 2-D and 3-D SEM model.

| Elastic modulus (GPa) | Poisson's ratio | Density (kg/m$^3$) |
|---|---|---|
| 69 | 0.31 | 2700 |

269

270    Table 3. Theoretical phase and group velocities of guided wave.

| Frequency (kHz) | Phase velocity $A_0$ (m/s) | Group velocity $A_0$ (m/s) | Wavelength (mm) |
|---|---|---|---|
| 20 | 435.9975 | 855.2961 | 21.8 |

| 100 | 947.6198 | 1770.3762 | 9.48 |

271

Take the displacement field as illustrated in Figure 6 for example, the fundamental symmetric

mode $S_0$ arrives earlier, followed by the slower fundamental anti-symmetric mode $A_0$. As the

concerned frequency $f_c = 100$ kHz is far below the cut-off frequency of $A_1$ mode, only $S_0$

and $A_0$ mode propagate in the plate structure. For brevity, only $A_0$ mode is investigated in this

paper. To calculate the wave propagation velocity, the out-of-plane displacements of both the

top and bottom nodes A and B at the same in-plane position of cross section A-B are extracted

and added to isolate the $A_0$ mode (Figure 7) expressed as

$$u_{\eta A,B}^{(a)}(t) = \frac{u_\eta^A(t) + u_\eta^B(t)}{2}, \tag{10}$$

which, through Hilbert transform, converts to the wave packet $e_{A,B}^{(a)}$. Then the wave arrival time

$t_{A,B}^{(a)}$ is calculated as

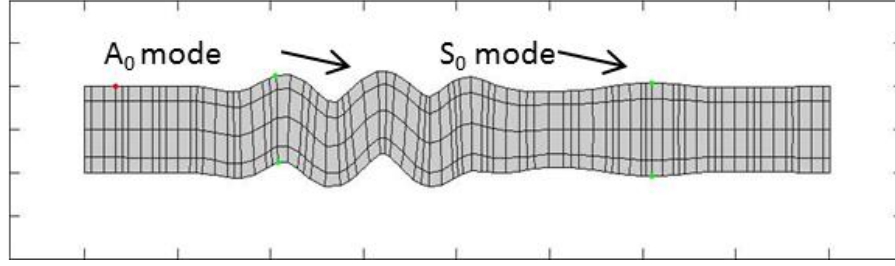$$t_{A,B}^{(a)} = \frac{\int_0^{t_{end}} e_{A,B}^{(a)}(t) \cdot t \, dt}{\int_0^{t_{end}} e_{A,B}^{(a)}(t) \, dt}, \tag{11}$$

Likewise, the $A_0$ mode at the section C-D is also isolated, whereby the wave group velocity

can be thus calculated as

$$c_{g,c}^{(a)} = \frac{c - b}{t_{CD}^{(a)} - t_{AB}^{(a)}}. \tag{12}$$

The error between the calculated group velocity $(c_{g,c}^{(a)})$ and theoretical group velocity $(c_{g,t}^{(a)})$

(Table 3) is expressed as

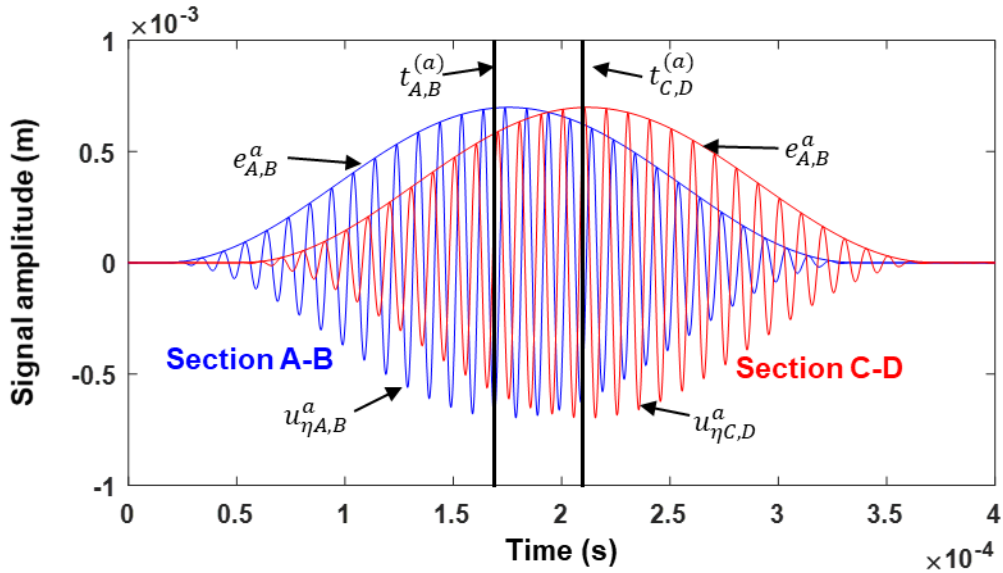$$error = \frac{|c_{g,c}^{(a)} - c_{g,t}^{(a)}|}{c_{g,t}^{(a)}}. \tag{13}$$

289

Figure 6. Typical displacement response containing $A_0$ and $S_0$ modes (the scale of displacement and coordinate in the in-plane and out-of-plane direction is adjusted for illustration).



Figure 7. Displacement signal and wave packet at sections A-B and C-D to extract time of arrival $t_{A,B}^{(a)}$ and $t_{C,D}^{(a)}$.

### 3.2 Results and Discussions

To explore the limit of accuracy using SEM to simulate wave propagation, as well as to provide a benchmark to associate the accuracy with mesh parameter, several sets of numerical simulation with varying parameters $n_\lambda$ (1~20), $p_\xi$ (1~5) and $p_\eta$ (1~4) are performed using the model as detailed in Section 3.1.

305   Take the case with central frequency $f_c = 100$ kHz as example. In the first set of simulation,

306   $p_\eta$ is set as 1, the relation of calculation error with in-plane parameter is studied. Figure 8 (a)

307   displays the calculated error of $A_0$, which exhibits a trend of decrease as the increase of $n_\lambda$ or

308   $p_\xi$. Nevertheless, the minimum error can only reach around 2% despite the dense in-plane node

309   collation $n_\lambda = 20$ and high polynomial order $p_\xi = 5$.

310

311   Another set of simulation ensues, in which $p_\eta$ is set as 4 to guarantee the accuracy in the

312   thickness direction. Notably, the minimum error decreases drastically to 0.03%, a remarkable

313   improvement of calculation accuracy compared with $p_\eta = 1$. Thus it is easily concluded that

314   the polynomial order $p_\eta$ decides the minimum calculation error that can be achieved. And only

315   when $n_\lambda$ and $p_\xi$ are large enough, the minimum calculation error can be realized. Another

316   noticeable phenomenon is that when $n_\lambda = Np_\xi, (N = 1, 2)$, such as $n_\lambda = 2p_\xi = 8$ in Figure 8

317   (b), and $n_\lambda = 2p_\xi = 6$ in Figure 8 (a) and (b), the error abruptly increases, which is yet to be

318   explained in the future research.

319

320   Following the above similar ideas, $p_\eta$ is further set as 2 and 3, respectively. Summarizing all

321   the obtained results, the relation of minimum calculation error with polynomial order in the

322   thickness direction $p_\eta$ is obtained in Figure 9, which indicates a monotonous improvement of

323   calculation accuracy with the increase of $p_\eta$. This benchmark helps selection of $p_\eta$ given a

324   pre-required calculation accuracy, which will be adopted for 3-D models in Section 4. The last

325   point to stress is that the obtained benchmark above can only be applied to the specified scenario

326   of $A_0$ mode, which means that if higher modes $A_i$ $(i = 1,2,3 \dots)$ or $A_0$ at a much higher

327   frequency are concerned, the benchmark in the thickness direction should be rebuilt. The

328   explanation goes as follows: on one hand, taking the fundamental $A_0$ for example, when the

329 frequency-thickness product increases, the mode shape along the thickness direction gets

330 distorted, which requires more nodes and higher polynomial order in the thickness direction to

331 approximate accurately the mode shape; on the other hand, if higher modes are concerned, they

332 present more severe distortion of mode shape compared with fundamental mode. Contrary to

333 the rebuilding of the benchmark in the thickness direction, the benchmark in the propagation

334 direction (Figure 8) holds for all the modes under different frequency-thickness product values,

335 as the parameters $n_\lambda$ and $p_\xi$ are irrelevant to the mode shape in the thickness direction.

336

337
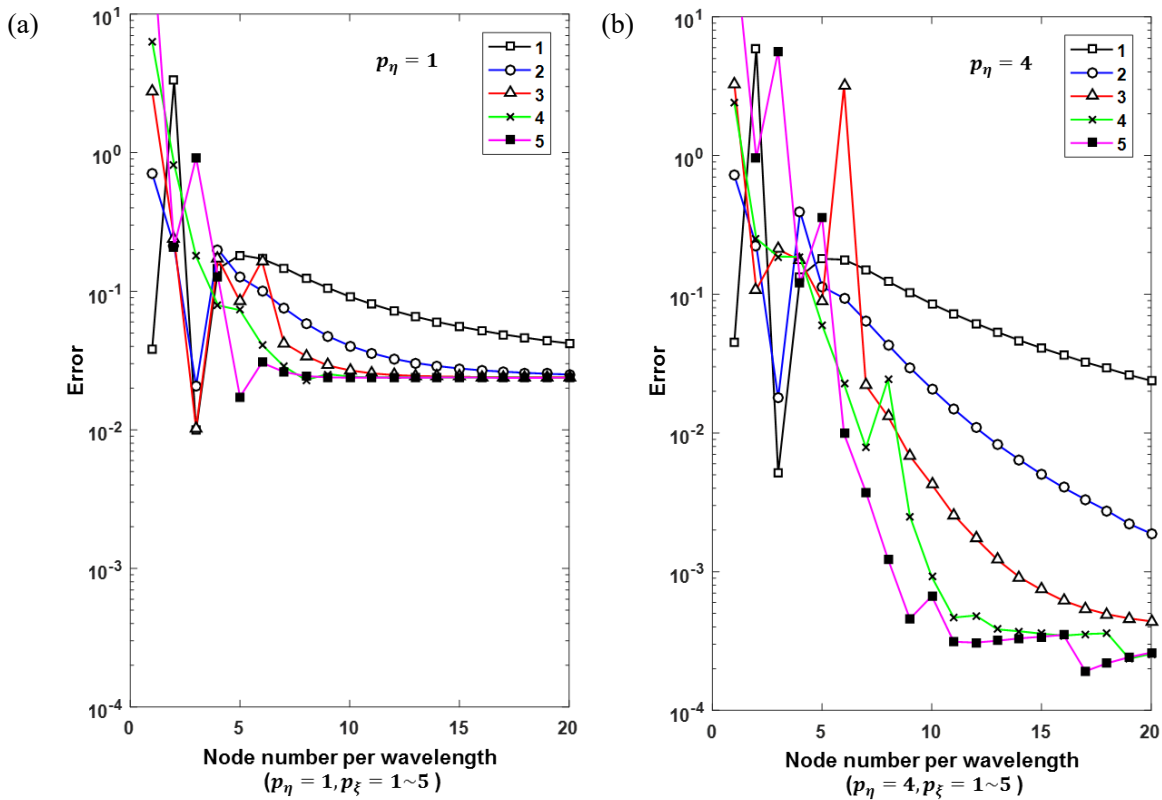


338 Figure 8. Benchmark study of calculated error of $A_0$ mode using SEM ($n_\lambda = 1\sim20, p_\xi =$

339 $1\sim5$): (a) $p_\eta = 1$, and (b) $p_\eta = 4$.

340

341
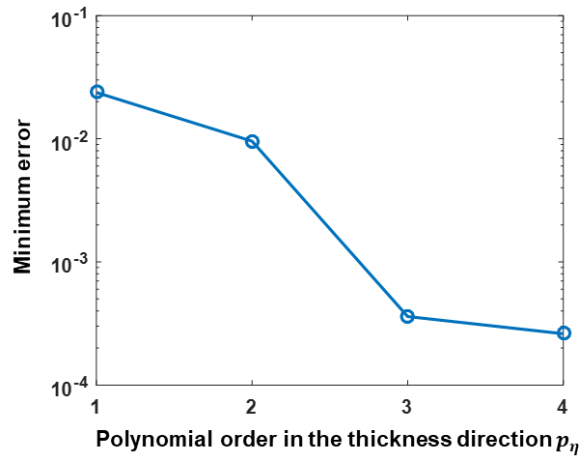


Figure 9. Benchmark study between minimum calculation error and polynomial order in the thickness direction $p_\eta$.

Besides the calculation accuracy, the calculation efficiency is another important factor for the evaluation of the feasibility of developed SEM. The calculation efficiency in terms of memory consumption and calculation time is displayed in Figure 10, in which $p_\eta$ is fixed as 4, to allow the variation of $p_\xi$ and $n_\lambda$. The consumed memory is linearly proportional to $n_\lambda$ with fixed $p_\xi$, which is easily explained as the total node number is linearly proportional to $n_\lambda$. The increased memory consumption with the increase of $p_\xi$ provided a fixed $n_\lambda$ can be attributed to the increase of nonzero element in the stiffness matrix. The calculation time, however, shows a nearly quadratic dependence to $n_\lambda$, as it is a combined effort of the number of nonzero element in the stiffness matrix and the number of time step in the entire calculation. The latter is inversely proportional to the length of each time increment, which decreases as the decrease of distance between two adjacent nodes. Provided the same $n_\lambda$, the calculation time shows a nearly linear increase as the increase of $p_\xi$, as only the number of nonzero element increases, while the distance between two adjacent nodes remains almost the same.

(a)



(b)
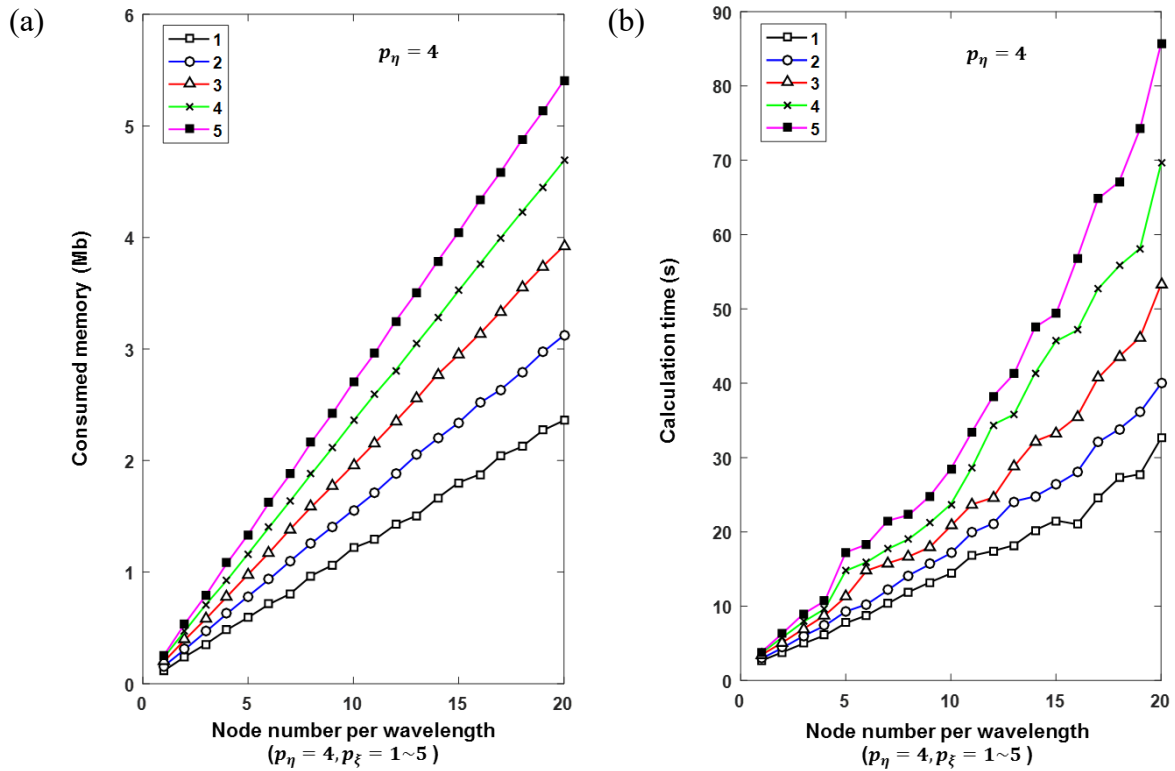


Figure 10 Comparison of (a) consumed memory and (b) calculation time of $A_0$ mode under 100 kHz using SEM ($n_\lambda = 1 \sim 20, p_\xi = 1 \sim 5$ $p_\eta = 4$).

## 4.    3-D SEM Model of Wave Scattering from Through Hole

A 3-D model of wave scattering from a through hole, as an example of the developed SEM model allowing arbitrary in-plane geometry, is built in this section to validate the correctness of the 3-D SEM model.

### 4.1    Model Description

Following the procedure in Section 2.3, a 3-D SEM model of wave scattering from a through hole is built as sketched in Figure 11, which is the same as [24] for a quantitative comparison with both experiments and analytical results. A through hole of Ø20 mm is drilled on an aluminum plate with dimensions $1000 \times 1000 \times 1$ mm$^3$. An out-of-plane force loading is applied at a point that has a distance of 300 mm to the center of the through hole. Only the left

373    half model is built in SEM, considering the symmetry of whole model. Two 10-cycle Hanning-

374    window-modulated sinusoidal signals with central frequencies $f_c = 20$ kHz and $100$ kHz are

375    acted as the out-of-plane loading respectively, which dominantly generate $A_0$ mode. According

376    to the theoretical wavelength listed in Table 3, it is set that $p_\xi = 2$, $p_\eta = 1$ and $n_\lambda = 10$ to

377    achieve an calculation error around 5%. This setting corresponds to the global mesh size of 0.4

378    mm and 0.2 mm for $f_c = 20$ kHz and $100$ kHz, respectively, in the ABAQUS® model. During

379    signal acquisition, the center of the through hole acts as the origin of a polar coordinate. The

380    normalized amplitude of the out-of-plane displacement at $r = 13$ mm from the center of the

381    through hole is extracted at angle $\psi$ from $0^0$ to $360^0$ at an interval of $5^0$. Here 'normalized'

382    means normalized with the amplitude of the incident wave without crossing the through hole.

383
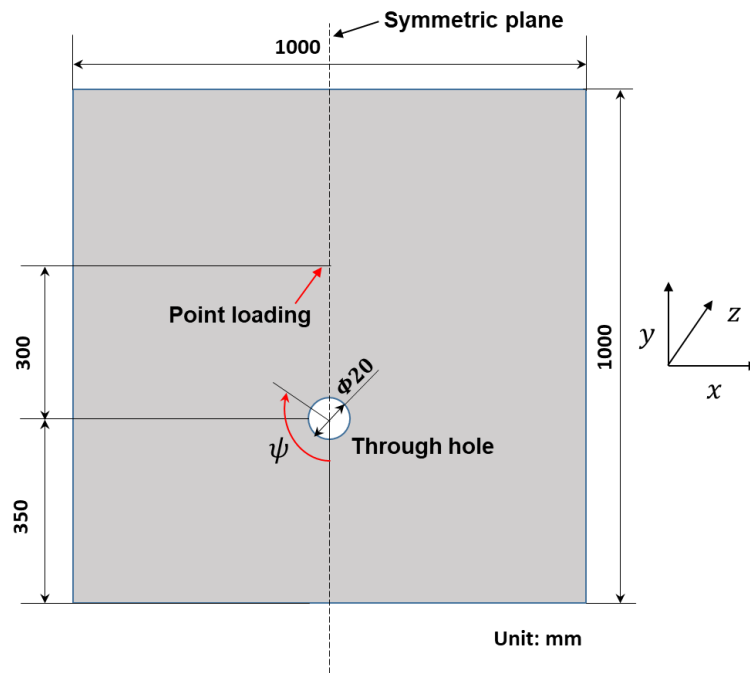


385    Figure 11. Sketch of $A_0$ mode crossing a through hole.

386

387    **4.2    Results and Discussions:**

388    4.2.1 $\boldsymbol{f_c = 20}$ **kHz**

389    The out-of-plane displacement amplitude when the incident $A_0$ mode of $f_c = 20$ kHz scatters

390  from the through hole based on the calculation using SEM is shown in Figure 12, to compare

391  with the analytical results based on classical plate theory (CPT), whose derivation is explained

392  in detail [24]. The magnitude obtained based on SEM and CPT at the angle close to $0^0$ shows a

393  relatively large discrepancy, which can be attributed to differences between simulation and

394  analytical assumption, i.e., a point force-generated circular wave versus straight-crested wave

395  and a 10-cycle modulated sinusoidal excitation versus a continuous sinusoidal excitation.

396  Overall speaking, the good match of the two sources of result at most angles, especially at

397  angles that face the incident waves, together with experiment measurement result [24], validates

398  the correctness of the developed SEM model.

399
400
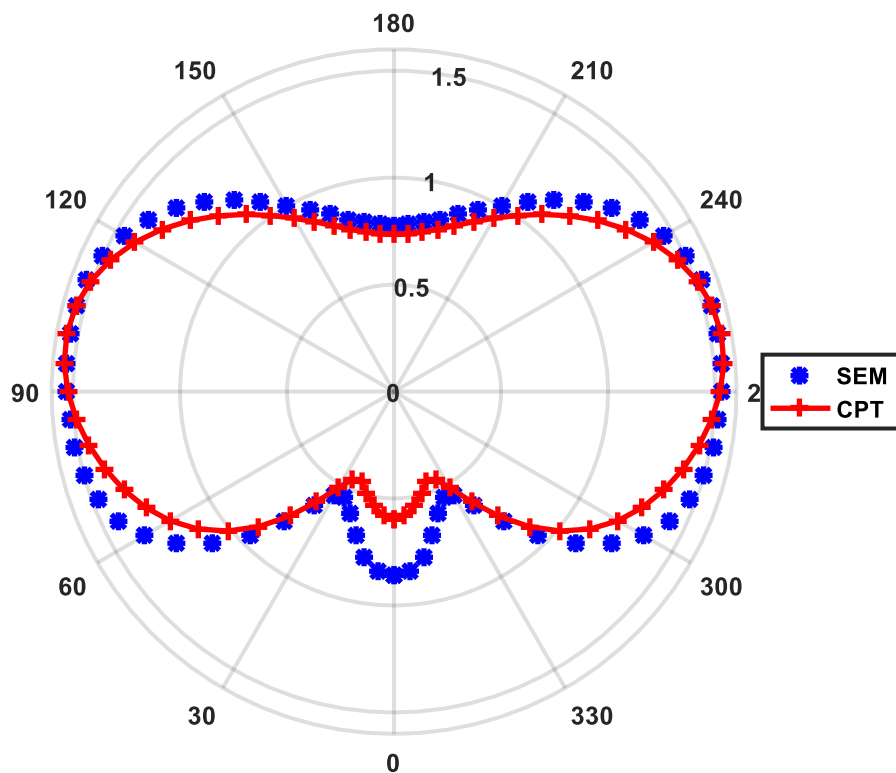


401  Figure 12. Amplitude (normalized) on a circle around the cavity based on SEM (spectral

402  element method) and CPT (classical plate theory): theta direction: $\psi$, radial direction: normalized

403  amplitude; plate thickness 1 mm, hole radius $r_0 = 10$ mm, signal acquisition at $r = 13$ mm,

404  frequency $f_c = 20$ kHz.

405

## 4.2.2 $f_c = 100$ kHz

When $f_c$ increases to 100 kHz, the wave scattering of incident $A_0$ encountering the through hole is also analyzed. Although Mindlin plate theory is preferred over CPT for the analysis of wave with higher frequency in [24] to take the shear and rotatory moment into consideration, the displayed error between Mindlin plate theory and CPT is small in [24]. Thus CPT is still adopted here to give analytical result, to be compared with SEM result (Figure 13). The comparison of the result, together with the experiment measurement in [24] holds the same conclusion. The magnitude obtained based on SEM and CPT at the angle close to $0^0$ shows a relatively large discrepancy, which can be attributed to the reasons explained in the Section 4.2.1. Overall speaking, the good match of the two sources of result at most angles, especially at angles that face the incident waves, together with experiment measurement result [24], validates the correctness of the developed SEM model.
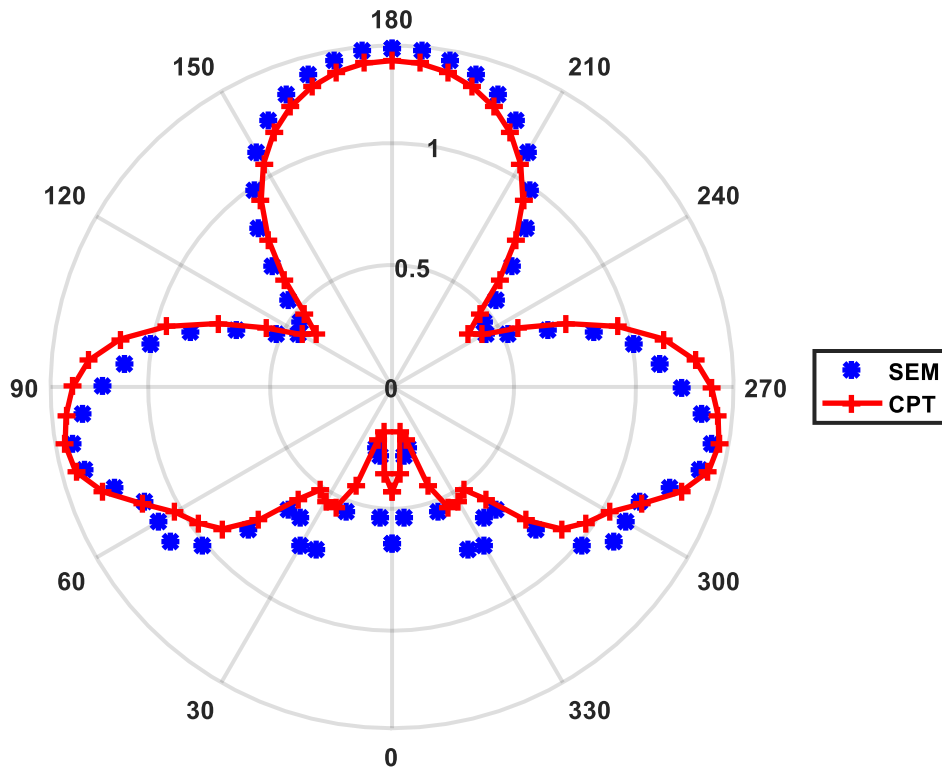


Figure 13. Amplitude (normalized) on a circle around the cavity based on SEM (spectral

421     element method) and CPT (classical plate theory): theta direction: $\psi$, radial direction: normalized

422     amplitude; plate thickness 1 mm, hole radius $r_0 = 10$ mm, signal acquisition at $r = 13$ mm,

423                      frequency $f_c = 100$ kHz.

424

## 5.     Conclusion

426 A benchmark study of accuracy and efficiency of SEM for modeling propagation of Lamb wave

427 is conducted in this research. In SEM, the GLL-based node collation, together with Lobatto

428 quadrature, intrinsically generates a diagonal mass matrix, which sets the roots for the superior

429 performance of SEM. The obtained error of group velocity using SEM can reach 0.03% for $A_0$,

430 proven to be an accurate simulation tool for wave propagation. To bring SEM into a useful tool

431 to model complex geometry, a 3-D SEM model with arbitrary in-plane geometry is developed,

432 whose correctness is validated through a model of $A_0$ mode scattering from a through hole.

433 Further development of the 3-D SEM model is on the way to include composite material and

434 defect such as delamination into consideration.

435

441

**References**

443 [1] Kundu, T., 2014, "Acoustic source localization," Ultrasonics, 54(1), pp. 25-38.

444 [2] Su, Z., Ye, L., and Lu, Y., 2006, "Guided Lamb waves for identification of damage in

445 composite structures: A review," Journal of Sound and Vibration, 295(3), pp. 753-780.

446 [3] Raghavan, A., and Cesnik, C. E., 2007, "Review of guided-wave structural health

447 monitoring," Shock and Vibration Digest, 39(2), pp. 91-116.

448 [4] Qiu, L., Yuan, S., Chang, F.-K., Bao, Q., and Mei, H., 2014, "On-line updating Gaussian

449 mixture model for aircraft wing spar damage evaluation under time-varying boundary

450 condition," Smart Materials and Structures, 23(12), p. 125001.

451 [5] Qiu, L., Yuan, S., Zhang, X., and Wang, Y., 2011, "A time reversal focusing based impact

452 imaging method and its evaluation on complex composite structures," Smart Materials and

453 Structures, 20(10), p. 105014.

454 [6] Zhou, C., Su, Z., and Cheng, L., 2011, "Quantitative evaluation of orientation-specific

455 damage using elastic waves and probability-based diagnostic imaging," Mechanical Systems

456 and Signal Processing, 25(6), pp. 2135-2156.

457 [7] Liu, M., Wang, Q., Zhang, Q., Long, R., and Su, Z., 2018, "Characterizing hypervelocity

458 (>2.5 km/s)-impact-engendered damage in shielding structures using in-situ acoustic emission:

459 Simulation and experiment," International Journal of Impact Engineering, 111(Supplement C),

460 pp. 273-284.

461 [8] Qiu, L., Liu, M., Qing, X., and Yuan, S., 2013, "A quantitative multidamage monitoring

462 method for large-scale complex composite," Structural Health Monitoring, 12(3), pp. 183-196.

463     [9] Giurgiutiu, V., 2007, Structural health monitoring: with piezoelectric wafer active sensors,

464     Academic Press.

465     [10] Cho, Y., and Rose, J. L., 1996, "A boundary element solution for a mode conversion study

466     on the edge reflection of Lamb waves," The Journal of the Acoustical Society of America, 99(4),

467     pp. 2097-2109.

468     [11] Alleyne, D. N., and Cawley, P., 1992, "The interaction of Lamb waves with defects," IEEE

469     Transactions on Ultrasonics, Ferroelectrics, and Frequency control, 39(3), pp. 381-397.

470     [12] Sundararaman, S., and Adams, D. E., 2008, "Modeling guided waves for damage

471     identification in isotropic and orthotropic plates using a local interaction simulation approach,"

472     Journal of Vibration and Acoustics, 130(4), p. 041009.

473     [13] Shen, Y., and Cesnik, C. E., 2017, "Modeling of nonlinear interactions between guided

474     waves and fatigue cracks using local interaction simulation approach," Ultrasonics, 74, pp. 106-

475     123.

476     [14] Shen, Y., and Giurgiutiu, V., 2016, "Combined analytical FEM approach for efficient

477     simulation of Lamb wave damage detection," Ultrasonics, 69, pp. 116-128.

478     [15] Patera, A. T., 1984, "A spectral element method for fluid dynamics: laminar flow in a

479     channel expansion," Journal of computational Physics, 54(3), pp. 468-488.

480     [16] Komatitsch, D., and Vilotte, J.-P., 1998, "The spectral element method: An efficient tool to

481     simulate the seismic response of 2D and 3D geological structures," Bulletin of the

482     Seismological Society of America, 88(2), pp. 368-392.

483     [17] Komatitsch, D., Erlebacher, G., Göddeke, D., and Michéa, D., 2010, "High-order finite-

484     element seismic wave propagation modeling with MPI on a large GPU cluster," Journal of

485     Computational Physics, 229(20), pp. 7692-7714.

486     [18] Kudela, P., Żak, A., Krawczuk, M., and Ostachowicz, W., 2007, "Modelling of wave

487     propagation in composite plates using the time domain spectral element method," Journal of

488     Sound and Vibration, 302(4), pp. 728-745.

489     [19] Zak, A., Krawczuk, M., and Ostachowicz, W., 2006, "Propagation of in-plane waves in an

490     isotropic panel with a crack," Finite Elements in Analysis and Design, 42(11), pp. 929-941.

491     [20] Peng, H., Meng, G., and Li, F., 2009, "Modeling of wave propagation in plate structures

492     using three-dimensional spectral element method for damage detection," Journal of Sound and

493     Vibration, 320(4–5), pp. 942-954.

494     [21] Żak, A., and Krawczuk, M., 2011, "Certain numerical issues of wave propagation

495     modelling in rods by the Spectral Finite Element Method," Finite Elements in Analysis and

496     Design, 47(9), pp. 1036-1046.

497     [22] Rose, J. L., 2014, Ultrasonic guided waves in solid media, Cambridge University Press.

498     [23] Taylor, R. L., 1972, "On completeness of shape functions for finite element analysis,"

499     International Journal for Numerical Methods in Engineering, 4(1), pp. 17-22.

500     [24] Fromme, P., and Sayir, M. B., 2002, "Measurement of the scattering of a Lamb wave by a

501     through hole in a plate," The Journal of the Acoustical Society of America, 111(3), pp. 1165-

502     1170.

503